Rodríguez-Sánchez, M. R., Marugán-Cruz, C., Acosta-Iborra, A. & Santana, D. (2018). Thermo-mechanical modelling of solar central receivers: Effect of incident solar flux resolution. *Solar Energy*, 165, pp. 43–54.

DOI: 10.1016/j.solener.2018.03.005

Thermo-mechanical modelling of solar central receivers: effect of incident solar flux resolution

M.R. Rodríguez-Sánchez[1, a)], C. Marugán-Cruz[1], A. Acosta-Iborra[1], D. Santana[1]

[1] *Energy Systems Engineering Group (ISE). Department of Thermal and Fluids Engineering from Universidad Carlos III de Madrid. Av. Universidad 30, Leganés, 28911 Madrid (Spain).*

a) Corresponding author: mrrsanch@ing.uc3m.es

Graphical abstract

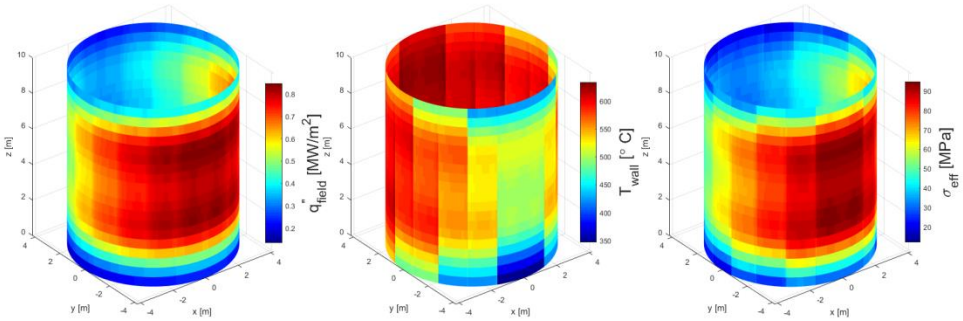

Abstract

The most important constraint for central receiver design is to keep the intercepting solar flux within the tube mechanical safety limits. An error in the heliostat aiming strategy or an inaccurate estimation of the tube temperature can produce overheating of the tubes, putting at risk the power plant operation. Therefore, the development of thermo-mechanical models to predict the incident solar flux, the temperature and the thermal stresses is mandatory.

The large number of tubes in the receivers makes a detailed simulation computationally expensive, and simplifications are usually done. These simplifications consist on selecting a representative tube in each panel of the receiver and reducing the spatial resolution of the incident radiation to a scale equal to one panel size. This "*coarse grid model*" simulation can be used with confidence to obtain the solar tower yield production with an error lower than 2.5%. However, the small resolution of this model results in errors in the wall temperature and the thermal stresses estimation, and hence in the aiming strategy selection.

In this study a "*fine grid model*", whose cells have a size equal to the tube pitch (distance between centres of the tubes) width in the receiver, has been developed for an accurate estimation of the tube wall temperature. Using this *fine grid model* the temperature and the

thermal stress profiles in each tube, for a given panel of the receiver, can be indirectly obtained without assuming that all the tubes of the panel have the same temperature profiles. Therefore, for modelling receiver, the *fine grid model* is required to determine with more accuracy the maximum tube stress and the aiming strategy, especially in the real situation of a highly non-uniform solar flux onto the receiver.

Key words

Solar power tower; Solar external receiver; Fine grid model; Thermo-mechanical analysis.

Nomenclature

Abbreviations

CFD: Computational fluid dynamics

CGM: Coarse grid model

e : East

FGM: Fine grid model

HTF: Heat transfer fluid

N: North

p : Panel

RAM: Random Access Memory

RW: Refractory wall

S: South

SPT: Solar power tower

Surr: Surroundings

t : Tube

w : West

Symbols

c : Specific heat [J/kgK]

d : Diameter [m]

E : Young's modulus [Pa]

F : View factor [-]

H : Receiver height [m]

h : Convective coefficient [W/m^{2}K]

k : Aim factor [-]

k_t : Thermal conductivity [W/mK]

m : Discrete circumferential coordinate [-]

$\dot{m}$: Mass flow rate [kg/s]

n : Discrete axial coordinate [-]

N_i : Number of elements [-]

pr : Perimeter [m]

q'' : Heat flux [W/m^2]

R''_f : Fouling resistance [m^{2}K/W]

s : Number of iterations [-]

T : Temperature [K]

U : Global heat transfer coefficient [W/m^{2}K]

v : Velocity [m/s]

z : Axial coordinate [m]

α : Absorptivity [-]

δ : Kronecker delta [-]

ε : Emissivity

γ : Thermal expansion coefficient [1/K]

η : Efficiency [-]

θ : Circumferential coordinate [°]

σ_B : Stefan Boltzmann constant [W/m^{2}K^4]

σ_{eff} : Thermal stress [Pa]

υ : Poisson's coefficient [-]

Subscripts

amb : Ambient

ext : External

fp : Flow path

int : Internal

rec : Receiver

$Surr$: Surroundings

1. Introduction

Renewable energy is currently acknowledged as the most feasible option required to both reduce the CO_2 emissions and to achieve sustainable development in a near future. The main problem of renewable energy is that it depends on a natural source (wind, waves, sun, etc.) and it cannot easily be adapted to the demand of the electricity market; thus it cannot stand alone. The renewable technology with the highest degree of dispatchability is the thermo-solar technology with thermal storage, within this technology Solar power towers (SPT) are particularly relevant (Gauché et al., 2017). Nowadays, SPT technology is not cost-competitive against fossil power plants or other renewables energies, such as wind or photovoltaic energy (Hernández-Moro and Martínez-Duart, 2013). However, the development of SPT is essential for the deployment of renewable energies as baseload plants (Lilliestam et al., 2017).

Solar receivers, which are the most critical subsystems of SPTs, are subjected to extreme working conditions. On their outer face, the tubes of the receivers intercept the concentrated solar radiation reaching high temperature, while the inner face of the tubes is refrigerated by a heat transfer fluid that can be corrosive, e.g. molten salt. Direct measurement of the incident solar flux and of the wall temperature during receiver operation is impracticable. Thus it is essential to develop thermal and mechanical models to analyse the receiver behaviour and control the plant operation (Garcia et al., 2008).

Two are the main simulation techniques used in the design and analysis of solar power plants: simulation using detailed models and simulations based on simplified models (Behar et al., 2013). Detailed models give a high temporal and spatial resolution of the variables (temperature, velocity, solar flux distribution, etc.) and they are restricted to specific elements of the facility, as for example, the panel manifold. Detailed simulation uses multi-physics models that couple the fluid motion with other physical processes such as the heat transfer in solids or the external radiation. Nowadays, detailed simulations of a complete solar power plant are

unfeasible due to the great disparity of scales and the numerous physical processes that take place, which makes the CFD models too computationally expensive (Rodríguez-Sánchez et al., 2014a).

The simplified models seek to understand the macroscopic operation of the power plants, renouncing to show in detail most of the variables. These models integrate a huge number of elements, recreating complex elements of the plant with low computational cost. Usually, these models are semi-empirical, using correlations or integral balances of mass and energy. The last generation of simplified models combines the macroscopic analysis of the power plant with the specific simulation of certain parameters, whose description is crucial to reproduce the plant operation. The development of these models provides paramount information for the analysis of the solar receivers (Li et al., 2017).

Previous works devoted to the analysis of the thermo-structural behaviour of central receivers have considered that the flux density that reaches a receiver can be described with a spatial resolution equal to the size of the receiver panel. These models will be referred here as a '*coarse grid model*' (CGM). Although relevant results can be obtained with this procedure, a resolution of the flux density equal to the panel size is relatively coarse because it assumes that the flux distribution only changes from panel to panel but not from tube to tube of a given panel. However, in order to capture more precisely the temperature and the thermal stresses peaks of the tube receiver, a model capable of using a finer resolution of the incident flux density should be developed.

In this study the simplified thermal model developed in (Rodríguez-Sánchez et al., 2014b), which is a CGM that only considers one representative tube per panel, has been extended to calculate in detail the temperature and mechanical stresses distribution in every tube of a receiver. The resulting new model, whose resolution is equal to a tube pitch width (distance between centres of the tubes), will be named '*fine grid model*' (FGM) from now on. The model developed solves, in a simple way, the conjugate problem between the radiative and convective heat transfer on the tubes and the heat conduction in the tube walls. Besides, the FGM gives more precise information to quantify the heat power absorbed in the receiver, as well as the thermal and mechanical behaviour of each tube in the receivers. This model has been devised for molten salt as heat transfer fluid (HTF), although it could be applied to other HTFs.

This paper is organized as follows: in the following section the 'fine grid model' is described. In section 3 the geometry parameters of the prototype receiver used for carrying out the analysis are described. In section 4 a comparison between the CGM and the FGM predictions on the

thermal and structural behaviours of the receiver is done. This comparison is focused to the ideal case of homogenous incident solar flux distribution on the receiver and to the more realistic cases of non-uniform flux distribution resulting from different aiming strategies. Finally, section 5 presents the main conclusions of this study.

2. Receiver model

To analyse the thermo-structural behaviour of the external receivers a new method based on the thermal model proposed in (Rodríguez-Sánchez et al., 2014b) has been developed in the present work. This new method, which can be named *fine grid model* (FGM, as mentioned before), includes all the tubes of the receiver and not only one representative tube per panel (*coarse grid model,* CGM). Each tube is exposed to a different radiation heat flux, which results in a different wall temperature distribution. As a consequence, the FGM can yield more accurate estimations of the heat absorbed by the receiver, the tube wall temperature distribution and the thermal stresses of the receiver compared to a CGM.

Therefore, the aim of the FGM proposed in this work is to improve the accuracy of the thermo-mechanical models through the resolution of a complete receiver, preserving the advantages of simplified models, i.e. the low computational cost (Rodríguez-Sánchez et al., 2014a). The following lines describe the FGM and how it improves simplified models (i.e. CGM) previously proposed in the literature.

Firstly, regarding the incident flux density on the receiver, in the CGM only two opposite half tubes (i.e. a basic cell) are studied and it is assumed that the solar flux intercepted by each tube, which forms part of a panel, is equal to the average flux on that panel, q''_{field} (Rodríguez-Sánchez et al., 2014a). That means that in the CGM identical performance is assumed for all the tubes in a panel, see Figure 1.a. However, in the FGM the incident flux density varies from tube to tube of a panel and all its tubes are simultaneously analysed, including the radiation interaction of the tubes with their closest tubes pertaining to the neighbour panels. Thus, the total number of basic cells in the FGM, each one receiving a different incident heat flux, $q''_{field,j}$, is equal to the number of tubes plus one, $N_t + 1$ (see Figure 1.b). The flux used in the CGM, q''_{field}, is the average of the incident heat fluxes on the basic cells of a panel in the FGM:

$$q''_{field} = \frac{\frac{q''_{field,0}}{2} + \sum_{j=1}^{N_t-1} q''_{field,j} + \frac{q''_{field,N_t}}{2}}{N_t} \qquad \text{Equation 1}$$

Where, N_t is the number of tubes in a panel and $q''_{field,j}$ is the incident heat flux on the basic cell comprising the opposite halves of tubes j and (j+1) of the panel. The methodology proposed by (Sánchez-González and Santana, 2015) has been integrated in the FGM to obtain the incident solar fluxes $q''_{field,j}$. Note that equation 1 has the factor ½ in the heat fluxes $q''_{field,0}$ and q''_{field,N_t} because in the CGM only half of the cells 0 and N_t pertains to a panel.

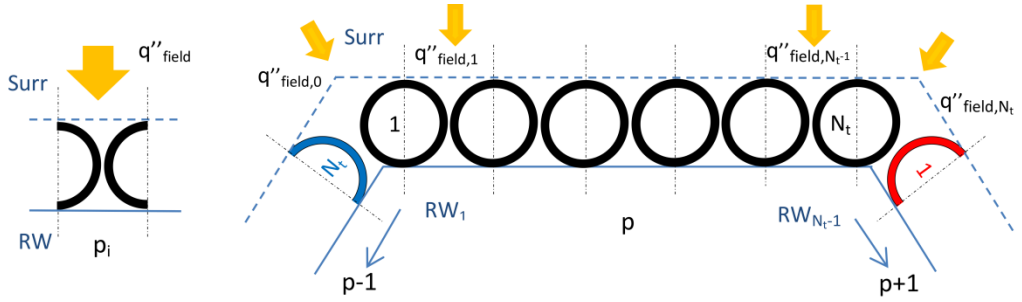

Figure 1 – Schematic representation of the basic cells used in the thermal model of a panel *p* of the receiver: (a) CGM, (b) FGM.

As in the CGM, the FGM considers that the basic cells are limited by two surfaces in addition to the tubes: an imaginary frontal surface, that represents the sky as well as the ground (i.e. the surroundings), and a real rear surface formed by a highly reflective refractory wall (RW) that is installed to reduce the thermal losses.

Secondly, the FGM divides each tube of a panel in axial segments and circumferential sections, as can be seen in Figure 2. Hence, all the variables of the tubes depend on the panel (denoted with index p), the tube (t), the axial length (z) and the circumferential position or angle index (θ). The properties of the refractory wall depend on (p,t,z), while the properties of the surroundings are constant. On the contrary, in the CGM these sections refer only to the two half tubes of the cell that are used to represent the whole panel (Rodríguez-Sánchez et al., 2014a) so that the results are not a function of the index t.

Thirdly, the radiative heat flux that is absorbed by the tubes, $q''(p,t,\bar{z},\theta)$, together with the fourth power of the temperature involved in radiation, $T^4(p,t,\bar{z},\theta)$, at the surface of the tube sections and at the refractory wall sections, are calculated in an iterative process using a radiative exchange balance that is obtained by the net radiation method (Modest, 2003). Conceptually, $q''(p,t,\bar{z},\theta)$ and $T^4(p,t,\bar{z},\theta)$ refer to the average value of the heat flux and temperature at the outer surface of a given section, where $\bar{z}$ is an integer index that indicates

the vertical position at the middle length of a section, see Figure 2 and 3. The resulting balance for a given section of indexes $(p,t,\bar{z},\theta)$ in a cell between two tubes of the same panel is:

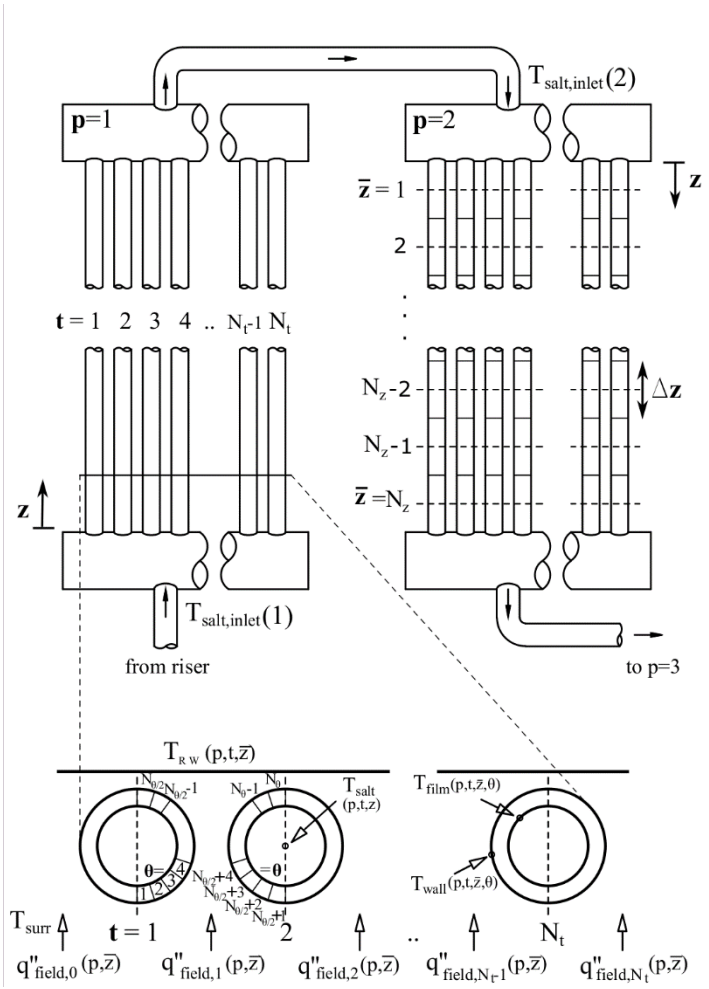

Figure 2- Schematic representation of two consecutive panels of the receiver showing the flow path, the main variables and the tube sections used in the model.

$$\left[\frac{\delta_{m,0}}{\varepsilon_0}-\left(\frac{1}{\varepsilon_0}-1\right)F_{m,0}\right]\frac{q_0''(p,t,\bar{z})}{\sigma_B}+\sum_{\theta=1}^{N_\theta}\left[\frac{\delta_{m,\theta}}{\varepsilon}-\left(\frac{1}{\varepsilon}-1\right)F_{m,\theta}\right]\frac{q''(p,t,\bar{z},\theta)}{\sigma_B}$$

$$-\left[\delta_{m,N_\theta+1}-F_{m,N_\theta+1}\right]T^4(p,t,\bar{z},N_\theta+1)=\left[\delta_{m,0}-F_{m,0}\right]T_{surr}^4+\sum_{\theta=1}^{N_\theta}\left[\delta_{m,\theta}-F_{m,\theta}\right]T^4(p,t,\bar{z},\theta) \quad \text{Equation 2}$$

$$-\left[\frac{\delta_{m,N_\theta+1}}{\varepsilon_{N_\theta+1}}-\left(\frac{1}{\varepsilon_{N_\theta+1}}-1\right)F_{m,N_\theta+1}\right]\frac{q''(p,t,\bar{z},N_\theta+1)}{\sigma_B}-F_{m,0}\frac{q''_{field,t}(p,\bar{z})}{\sigma_B}\alpha$$

Where $p=1,2,...,N_p/N_{fp}$ is the index referring to the panel in which the tube of the section is located, with N_p is equal to the total number of panels in the receiver and N_{fp} is equal to

the number of flow paths in the receiver, $t = 1,2,...,N_t$ is the index of the tube in a panel, $\bar{z} = 1,2,...,N_z$ is the index of the vertical location of the section taken in the flow direction, with $N_z = H/\Delta z$ equal to the number of segments in which a tube is divided axially, see Figure 2. The vertical size of the segments, Δz, is selected to be sufficiently small so that homogeneous 2D radiation can be assumed in vertical direction within each segment. In Equation 2 $m = 0,1,2,...,N_\theta + 1$ is the index used to number the different sections of the problem at a given $\bar{z}$ in which the balance is done, and $\theta = 1,2,...,N_\theta$ is the index of the location in circumferential direction of the tube section that interact with m, as shown in Figure 2. N_θ is selected to assure independence on the grid size, $\theta = N_\theta + 1$ corresponds to the refractory wall and $\theta = 0$ to the imaginary surface of the surroundings, whose equivalent temperature is:

$$T_{surr} = \sqrt[4]{\frac{\varepsilon_{sky} T_{sky}^4 + \varepsilon_{ground} T_{ground}^4}{\varepsilon_{sky} + \varepsilon_{ground}}} \Rightarrow \text{Constant} \qquad \text{Equation 3}$$

Where T_{sky} and ε_{sky} are equal to the effective radiation temperature and emissivity of the sky and T_{ground} and ε_{ground} correspond to the temperature and emissivity of the ground.

In equation 2, ε is the emissivity of the surface of each section, which is dependent of the surface temperature, σ_B is the Stefan-Boltzmann constant, $\delta_{i,j}$ is the Kronecker Delta, $F_{i,j}$ is the view factor between sections i and j and α is the absorptivity of the sections.

Similarly, the radiative heat balance for a cell between two consecutive panels (panel a and panel b) is:

$$\begin{aligned}
&\left[\frac{\delta_{m,0}}{\varepsilon_0} - \left(\frac{1}{\varepsilon_0} - 1\right) F_{m,0}\right] \frac{q''(p_a, t_a, \bar{z}_a)}{\sigma_B} + \sum_{\theta=1}^{N_\theta/2} \left[\frac{\delta_{m,\theta}}{\varepsilon_a} - \left(\frac{1}{\varepsilon_a} - 1\right) F_{m,\theta}\right] \frac{q''(p_a, t_a, \bar{z}_a, \theta)}{\sigma_B} \\
&+ \sum_{\theta=N_\theta/2+1}^{N_\theta} \left[\frac{\delta_{m,\theta}}{\varepsilon_b} - \left(\frac{1}{\varepsilon_b} - 1\right) F_{m,\theta}\right] \frac{q''(p_b, t_b, \bar{z}_b, \theta)}{\sigma_B} - \left[\delta_{m,N_\theta+1} - F_{m,N_\theta+1}\right] T^4(p_a, t_a, \bar{z}_a, N_\theta + 1) \\
&= \left[\delta_{m,0} - F_{m,0}\right] T_{surr}^4 + \sum_{\theta=1}^{N_\theta/2} \left[\delta_{m,\theta} - F_{m,\theta}\right] T^4(p_a, t_a, \bar{z}_a, \theta) + \sum_{\theta=N_\theta/2+1}^{N_\theta} \left[\delta_{m,\theta} - F_{m,\theta}\right] T^4(p_b, t_b, \bar{z}_b, \theta) \\
&- \left[\frac{\delta_{m,N_\theta+1}}{\varepsilon_{N_\theta+1,a}} - \left(\frac{1}{\varepsilon_{N_\theta+1,a}} - 1\right) F_{m,N_\theta+1}\right] \frac{q''(p_a, t_a, \bar{z}_a, N_\theta + 1)}{\sigma_B} \\
&- F_{m,0} \left[\frac{q''_{field,t_a}(p_a, \bar{z}_a)}{2\sigma_B} \alpha + \frac{q''_{field,t_b}(p_b, \bar{z}_b)}{2\sigma_B} \alpha\right]
\end{aligned}$$

Equation 4

Where the subscript a refers to the panel where the analysed cell is located and subscript b corresponds to the previous or the following panel. These indexes are related as follows: if $t_a = 1$ then $t_b = N_t$, and vice versa ($t_a = N_t$ and $t_b = 1$). Also, if $t_a = 1$ then $p_b = p_a - 1$ for $p_a = 1, 2, ..., \mathrm{N_p}/\mathrm{N_{fp}}$ (in the first panel $p_a = 1e$ and $p_b = N_p = 1w$, see Figure 6), else if $t_a = N_t$, then $p_b = p_a + 1$ for $p_a = 1, 2, ..., \mathrm{N_p}/\mathrm{N_{fp}}$ (in the last panel $p_a = \mathrm{N_p}/\mathrm{N_{fp}} = 9e$ and $p_b = \mathrm{N_p}/\mathrm{N_{fp}} + 1 = 9w$, see Figure 6). Besides, $m = 0, 1, 2, ..., N_\theta + 1$, $\overline{z}_a = 1, 2, ..., N_z$ and $\overline{z}_b = N_z - \overline{z}_a + 1$ because the salt in two neighbouring tubes of different panels flows in opposite direction, see Figure 2.

In Equations 2 and 4 the net radiative heat flux is divided in three components: i) the radiative heat flux absorbed by the tubes in the visible spectrum coming from the total solar flux reflected by the heliostats (terms that include q''_{field}). This incident radiation from the heliostats is distributed within the tube surfaces by means of the view factors, $F_{m,0}$. Besides Equations 2 and 4 contains ii) the radiative heat flux that is absorbed by a given section due to the radiation reflected by the other sections (terms that include $q''(p,t,\overline{z},\theta)/\sigma_B$), and iii) the radiative heat flux that is absorbed by a given section due to the radiation emitted by the other sections in the infrared spectrum (terms that include $T^4(p,t,\overline{z},\theta)$).

Equations 2 and 4 are iteratively solved for all the sections of all the tubes of all the panels of the receiver, starting with an approximation of the temperature of such sections. To reduce the computational time needed for convergence, this initial estimation of the temperature of the sections is calculated with the simplified homogeneous temperature model (CGM) that applies the mean incident radiation to all the tubes of a given panel (Rodríguez-Sánchez et al., 2014a).

Fourthly, as Equations 2 and 4 only consider radiative heat transfer, the convective heat losses must be subtracted from the absorbed radiative heat flux, $q''(p,t,\overline{z},\theta)$, to obtain the net heat flux absorbed by the tubes, $q''_t(p,t,\overline{z},\theta)$:

$$q''_t(p,t,\overline{z},\theta) = q''(p,t,\overline{z},\theta) - h_{ext}(p,t,\overline{z},\theta)(T_{wall}(p,t,\overline{z},\theta) - T_{amb}) \qquad \text{Equation 5}$$

Where $h_{ext}(p,t,\overline{z})$ corresponds to the convective coefficient (Siebers and Kraabel, 1984) between the outer surface of the tubes, at temperature $T_{wall}(p,t,\overline{z},\theta)$, and the ambient air at temperature T_{amb}.

Fifthly, the bulk temperature of the molten salt at the exit of each vertical segment of the tubes, $T_{salt}(p,t,z+\Delta z)$, is calculated using an energy balance:

$$T_{salt}(p,t,z+\Delta z) = T_{salt}(p,t,z) + \frac{\Delta z}{\dot{m}c_p}\sum_{\theta=1}^{N_\theta} q_t''(p,t,\bar{z},\theta)pr(\theta) \qquad \text{Equation 6}$$

Where c_p is the specific heat of the molten salt, which is calculated as a function of the mean temperature of the molten salt in each tube segment, $\dot{m}$ is the mass flow rate the molten salt in each tube, $pr(\theta)$ is the tube perimeter circumferentially covered by a section and $T_{salt}(p,t,z)$ is the bulk temperature of the molten salt at the inlet of the vertical segment of the tubes. Therefore, T_{salt} is evaluated at points in the vertical coordinate, z, that are staggered in vertical direction with respect to the centre of the section where q'' and T^4 are associated, see Figure 3.

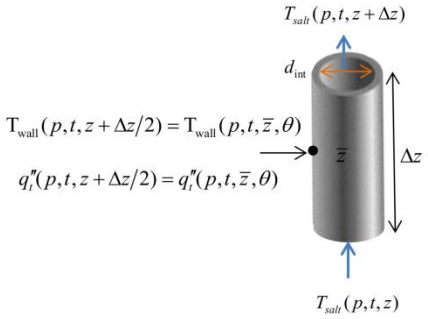

Figure 3 – Vertical segment of tube showing the different evaluation points used in the model.

Equation 6 can be calculated sequentially for any z starting from $T_{salt}(p,t,z=0) = T_{salt,inlet}(p)$, which is the temperature of the molten salt at the inlet of all the tubes of a given panel. Since the molten salt flows from one panel to the next one, see Figure 2, the temperature of the molten salt at the exit of all the tubes of a panel is averaged to calculate the temperature at the inlet of the tubes of the next panel,

$$T_{salt,inlet}(p+1) = \frac{\sum_{t=1}^{N_t} \dot{m}c_p T_{salt}(p,t,\mathrm{z}=H)}{\sum_{t=1}^{N_t} \dot{m}c_p} \qquad \text{Equation 7}$$

In Equation 7 heat loses associated at the inlet and exit collectors of the panels are neglected. Likewise, homogeneous distribution of the mass flow rate of molten salt through all the tubes can be assumed because the HTF properties do not change significantly to produce an uneven

pressure drop between the tubes of the same panel. It has been tested that the maximum pressure drop difference between tubes, under different conditions, is lower than 0.07%.

As the flow direction in the tubes changes from panel to panel, the exit of one panel and the inlet of the following panel are located at the same edge (top or bottom) of the receiver (see Figure 2). Therefore, the origin of axis *z* and the position of the inlet and outlet collectors change from one panel to the following.

Sixthly, the temperature at the outer surface of the tube and the film temperature (at the inner surface of the tube) are calculated for each section by means of following heat transfer relations:

$$T_{wall}(p,t,\overline{z},\theta) = \frac{1}{\Delta z}\int_{z}^{z+\Delta z}\left[T_{salt}(p,t,z) + \frac{q_t''(p,t,z,\theta)}{U(p,t,z,\theta)}\right]dz = T_{salt}(p,t,\overline{z}) + \frac{q_t''(p,t,\overline{z},\theta)}{U(p,t,\overline{z},\theta)} \quad \text{Equation 8}$$

$$T_{film}(p,t,\overline{z},\theta) = T_{wall}(p,t,\overline{z},\theta) - q_t''(p,t,\overline{z},\theta)\frac{d_{ext}\ln(d_{ext}/d_{\text{int}})}{2\,k_t} \quad \text{Equation 9}$$

Where $U(p,t,\overline{z},\theta)$ is the overall heat transfer coefficient involving conduction in the tube walls, fouling resistance at the inner surface of the tubes R_f'', and convection in the molten salt.

$$\frac{1}{U(p,t,\overline{z},\theta)} = \frac{d_{ext}\ln(d_{ext}/d_{\text{int}})}{2\,k_t} + \frac{d_{ext}R_f''}{d_{\text{int}}} + \frac{d_{ext}}{d_{\text{int}}\,h_{\text{int}}(p,t,\overline{z})} \quad \text{Equation 10}$$

In Equations 9 and 10, d_{ext} and d_{int} respectively express the outer and inner diameters of the tube wall, k_t is the thermal conductivity of the tube wall, calculated as a function of the tube wall temperature, and $h_{\text{int}}(p,t,\overline{z})$ is the convection coefficient of the molten salt calculated using Gnielinski's equation (Gnielinski, 2013). Inside the tubes the molten salt flow is fully turbulent because the Reynolds number is high enough. Thus, $h_{\text{int}}(p,t,\overline{z})$ can be considered independent of the angular coordinate (Yang et al., 2012).

The temperature involved in radiation can be then recalculated by spatially averaging the fourth power of the temperature at the outer surface of a given section:

$$T^4(p,t,\overline{z},\theta) = \frac{1}{\Delta z}\int_{z}^{z+\Delta z}\left[T_{salt}(p,t,z) + \frac{q_t''(p,t,z,\theta)}{U(p,t,z,\theta)}\right]^4 dz \quad \text{Equation 11}$$

Finally, in the FGM the calculation of variables with the above described equations is undertaken as follows.

The model requires the input data defining the geometrical parameters, the ambient and sky conditions (e.g. air and sky properties and wind velocity), the mass flow rate of molten salt in the tubes, the incident radiation with fine grid spatial resolution (i.e. $q''_{field,j}(p,\bar{z})$ with $j=1,2,...,N_t$ for each panel of the receiver) and the temperature of the molten salt at the inlet of the receiver, $T_{salt,inlet}(1)$, which is the inlet temperature of the tubes of the first panel (or of the two panels if the receiver has two parallel flow paths). The surroundings temperature is obtained with Equation 3. Then, an initial estimation the temperature at the outer surface of the walls, T_{wall}, is obtained by means of a CGM, which is the homogeneous temperature model described in (Rodríguez-Sánchez et al., 2014a). Therefore, the initial estimation of the wall temperature is $T^4(p,\mathrm{t},\bar{z},\theta)=\left(T_{CGM}(p,\bar{z},\theta)\right)^4$. With this initial value of temperatures (denoted as estimation s = 0), the system of Equations 2 and 4 is solved (e.g. by matrix inversion) to obtain the radiative heat fluxes that are absorbed by all the sections at a given height (z), for all the tubes, the reradiating wall and the equivalent surroundings surface of the first panel, $q''(\mathrm{p}=1,t,\bar{z},\theta)$. Wall properties are evaluated with the tube temperature in each section. Subsequently, the net heat flux absorbed by the tubes, $q''_t(p=1,t,\bar{z},\theta)$ is calculated with Equation 5, and the mean salt temperature at the outlet of each of the segments number z for all the tubes, $T_{salt}(p=1,t,z+\Delta z)$, is obtained with Equation 6. The properties of the molten salt are determined as a function of $T_{salt}(p=1,t,\bar{z})$ in each segment. Afterwards, Equations 8 to 10 are employed to evaluate $T_{film}(p=1,t,\bar{z},\theta)$, if needed, and to calculate $T_{wall}(p=1,t,\bar{z},\theta)$. Using Equation 11 the fourth power of the temperature at the outer surface of the sections, $T^4(p=1,t,\bar{z},\theta)$, is determined. The values of $T^4(p=1,t,\bar{z},\theta)$ are reintroduced to Equations 2 and 4 and all the process is repeated until convergence of the temperatures and heat fluxes for all the sectors at $\bar{z}=1$. Similarly, the process is repeated for all the segments, $\bar{z}=2,...,N_z$, of the tubes of the first panel. Then, the inlet temperature of the second panel, $T_{salt,inlet}(2)$, is obtained with Equation 7 and all the calculations are reproduced again, panel after panel ($p=2,3,...N_p$), up to the last panel of the receiver.

The above algorithm for the whole receiver is repeated using the results of $T^4(p,t,\bar{z},\theta)$ as the initial values of the next iteration (s=1) instead of the temperatures of the CGM. The iterations

of the whole receiver (s=2, 3, …) are stopped when the temperature and the radiation fluxes converge.

Figure 4 summarizes the calculation algorithm for the FGM proposed in the present work. For comparison, the algorithm of the CGM (Rodríguez-Sánchez et al., 2014a) has been included in Figure 5. As can be observed in the figures, the FGM introduces a dependence of the variables with the tube index, at the price of an additional iteration loop in the calculations. Nevertheless, the model is still quite fast when compared with other approaches such as CFD simulations.

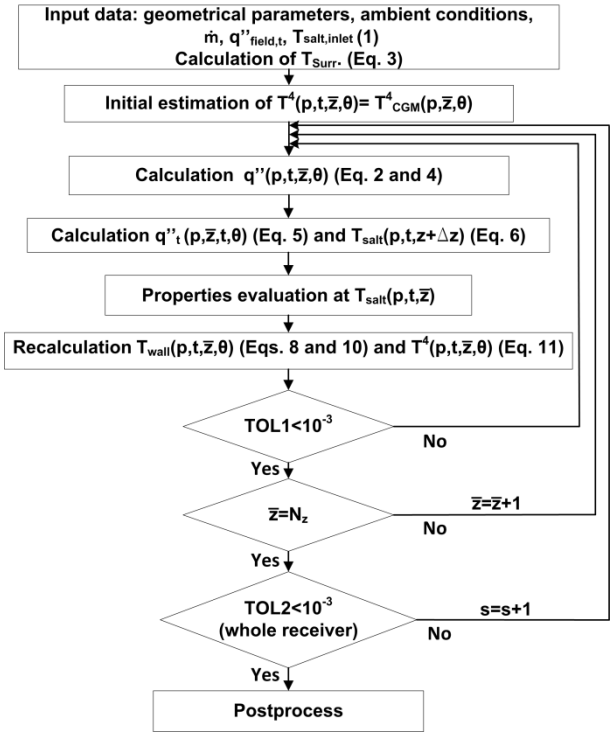

Figure 4- Calculating algorithm for the FGM. The equations numbers refer to the ones in Section 2.

Once the energy balance in the receiver is solved, the thermal efficiency of the receiver can be obtained. Here the thermal efficiency of the receiver is defined as the sum of the net absorbed heat on all the tubes of the receiver over the net heat reflected by the heliostats:

$$\eta_{rec} = \frac{\sum_{p=1}^{N_p}\sum_{t=1}^{N_t}\sum_{z=0}^{N_z}\sum_{\theta=0}^{N_\theta} q_t''(\mathrm{p,t},\bar{z},\theta)}{\sum_{p=1}^{N_p}\sum_{t=1}^{N_t}\sum_{z=0}^{N_z} q''_{field,t}(p,\bar{z})} \qquad \text{Equation 12}$$

Besides, once the temperature distribution of all the tubes of the receiver is known, the thermal stresses of the receiver due to the temperature gradients can be analysed. (Marugán-Cruz et al., 2016) showed that Gatewood's equation (Gatewood, 1940) should be used to calculate the

thermal stresses for a non-uniform heat flux through the tube walls. Besides, they showed that at a large Biot number (0.3-10), the thermal stresses predicted by Faupel and Fisher's equation (Faupel and Fisher, 1981) are qualitatively right and that the maximum thermal stresses occur on the side exposed to the heliostats. In our case, the value of the Biot number, $Bi = hd_{\text{int}} \ln(d_{ext}/d_{\text{int}})/(2k_t)$, is comprised between 0.66 and 0.79, and thus Faupel and Fisher's equation predicts the position of the maximum stress. Therefore, the following Gatewood's equation approximation can be used to calculate the effective thermal stresses (Nithyanandam and Pitchumani, 2016):

$$\sigma_{eff}(p,t,\bar{z},\theta) \approx \frac{\gamma E d_{ext}}{2(1-\upsilon)2k_t} q_t''(p,t,\bar{z},\theta) \ln\left(\frac{d_{ext}}{d_{\text{int}}}\right) \quad \text{Equation 13}$$

Where E, υ and γ are, respectively, the Young's modulus, the Poisson's ratio and the volumetric thermal expansion coefficient of the tube material, and all of them depend on the tube wall temperature.

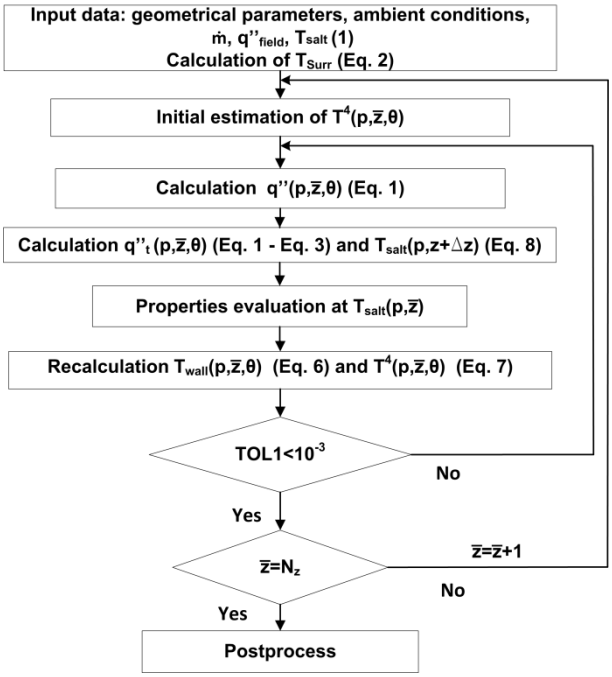

Figure 5- Calculating algorithm for the CGM. The equation numbers refer to (Rodríguez-Sánchez et al., 2014a).

3. Receiver geometry

The receiver prototype analysed in this work is similar to the one of Gemasolar, with a nominal thermal power of 120 MW_{th}. It is a cylindrical receiver 10 m height (H) and 8.5 m of diameter, which is composed by 18 vertical panels. Each panel has assembled 62 tubes of 2.21 cm of external dimeter and 1.97 cm of internal diameter. The tubes are made of Inconel 625 with

special thermal treatments that increase its elastic limits, and they are coated on its external surface with black Pyromark, which improves the solar absorption of the tubes.

The receiver is designed to work with solar salts (60% NaNO3 - 40% KNO3), that are heated from 290 °C ($T_{salt,inlet}(1)$) to 565 °C. At the inlet of the receiver, located in the north face of the receiver, the flow of molten salt is divided into two flow paths, each formed by 9 panels. Thus, in each flow path half of the mass flow rate goes through the nine panels, alternating direction from panel to panel like a serpentine. The flow of molten salt exits the receiver at the southern panel. The mass flow rate circulates in parallel in all tubes of a given panel. As it is pointed out in (Rodríguez-Sánchez et al., 2015), there are not crosses between flow paths.

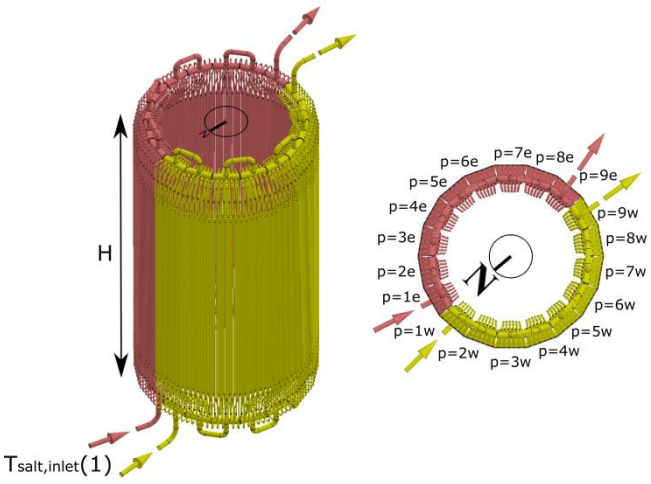

Figure 6 – Schematic representation of the receiver and molten salt flow configuration.

The mass flow rate of molten salt is a variable that depends on the incident solar flux and the mean temperature of the salt at the exit of the receiver. As commented in Section 2, the distribution of the mass flow rate in the tubes is assumed to be uniform.

Besides, Gemasolar solar field is radial staggered layout, which consists of 2,650 square heliostats of 10.95 m side. This layout is used to calculate the incident solar flux in the present work. The position of each heliostat has been determined with scaled aerial images of the SPTs.

Table 1 shows the value of the main parameters used to analyse the receiver. The molten salt and the Inconel 625 properties depend on the temperature and they are calculated with the correlations proposed by (Zavoico, 2001) and (American Society of Mechanical Engineers, 2011), respectively.

Table 1- Main parameters and ambient properties employed in the simulations

Variable	Value	Variable	Value
N_θ	74	ε_{RW}	0.2
N_z	20	ε_{sky}	0.85
$T_{salt,inlet}(1)$ [°C]	290	ε_{ground}	0.955
T_{amb} [°C]	25	α	0.95
T_{ground} [°C]	25	R''_f [m²K/W]	8.808e-5
T_{sky} [°C]	13.3	v_{wind} [m/s]	0

4. Results

Initially, to compare the results of the FGM and the CGM, a homogeneous incident solar radiation has been selected. This corresponds to the case in which the effect of the solar flux distribution is disregarded and the variation of temperature and thermal stresses from tube to tube are only due the heating of the molten salt. In a second step of the comparison, real incident solar fluxes have been considered for the analysis, to check the effect of the non-uniformity of the incident radiation on the results of the models.

4.1. Model comparison for the case of homogeneous heat flux

In CGM it is assumed that two adjacent tubes in a basic cell are at the same temperature. However, when analysing the receiver with FGM, two adjacent tubes could be at different temperature. This effect is especially noticeable in the edges of the panels, where two adjacent tubes correspond to consecutive panels, as will be seen in Figure 7. The effect of the salt temperature is important in the radiative heat exchanges, and then it affects to the whole efficient of the receiver. To analyse this effect, without the influence of the variation of the incident solar flux, a homogeneous incident flux of 0.3 MW/m^2 is employed in the whole receiver for the comparison of the CGM and the FGM at this section. In this case the two flow paths in the receiver (i.e. north-east-south and north-west-south) have the same behaviour and, for simplicity, only one of them is analysed.

Figure 7 shows the FGM results of circumferential profile of wall temperature at the outer surface of the first and last tubes of the second panel. The profiles are taken at three different vertical locations. For the sake of comparison, the circumferential profiles of the adjacent tubes have been also included in Figure 7. These profiles are only represented for an angle internal of 180° to differentiate them from the profiles of the first and last tubes of the second panel. In the second panel the flow goes downwards, and therefore the temperatures of the tubes

located in the first and second panels are similar at the top position. The temperature difference between the tube walls of the first and second panels increases from top to bottom, because the molten salt flow goes from bottom to top at the first panel and from top to bottom in the second panel. Thus, the temperature difference is the highest at the bottom. Therefore, the tube wall temperature of the first tube of the second panel is always higher than the temperature of the last tube of the previous panel. The opposite effect can be observed between the last tube of the second panel and the first tube of the third panel. Besides, it can be appreciated that due to the radiation exchange between adjacent tubes, the tube wall temperature of the tubes is not symmetric with respect to axis 0°-180°, and that there is a slightly temperature difference between the tubes of the same panel even for this case of homogenous incident heat flux.

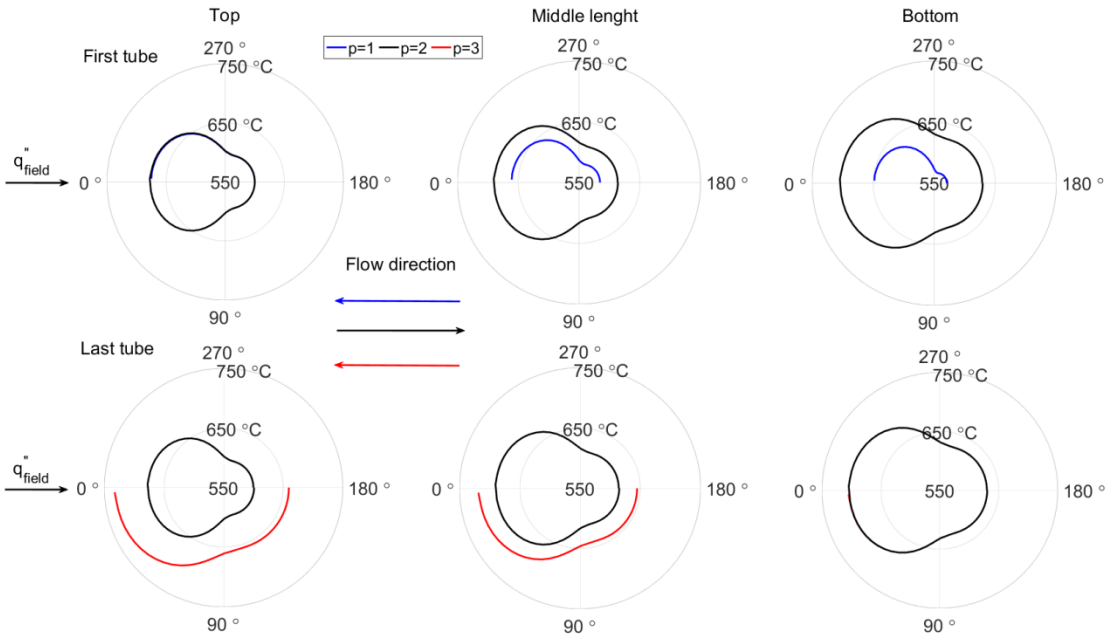

Figure 7- FGM circumferential profiles of wall temperature at the outer surface of the first and last tube of the second panel (p=2, black line) at three vertical locations for the case of a homogeneous solar radiation of 0.3 MW/m^2. For comparison, profiles spanning only 180° have been included, corresponding to the adjacent tubes, which can be located in the first (p=1, blue line) and third (p=3, red line) panel.

Each tube of the receiver influences in the behaviour of the other tubes, i.e. the radiation exchange between adjacent panels affects the wall temperature of several tubes per panel. This generates a difference in the mass flow rate when the tubes are studied individually (CGM) or in sets (FGM), resulting in 143.6 kg/s and 162.2 kg/s for CGM and FGM, respectively. Therefore, the receiver tubes cannot be calculated individually.

Figure 8 shows the maximum tube wall temperature of each tube obtained with both models under the conditions defined previously. As the heat flux is constant, the maximum temperature in each tube is reached at the exit edge. It can be observed that in the first panels the CGM predicts higher tube wall temperatures than the FGM, due to the minor refrigeration power of the solar salt that in the CGM flows at lower velocity. As in both cases the salt exits of the receiver at the same temperature, 565 °C, the wall temperature difference between models decreases along the receiver. However, the wall temperature in the last panel of the receiver is not the same for both models, the one estimated with the CGM being higher. Hence, the CGM underestimates the maximum wall temperature reached in the whole receiver (i.e. in the last panel) and, therefore, it underestimates the tube thermal stresses. This makes the CGM less accurate to predict failure of the tubes.

To show the effect of the interaction between panels revealed by the FGM, in Figure 8 a zoom of the second panel is shown. In this zoom it can be seen that in the first tube of the panel (accumulated tube number: N_t = 63) the maximum wall temperature is lower than in the tubes located in the middle of the panel, and that in the last tube of the panel (accumulated tube number: N_t =124) the maximum temperature is the highest of the panel. On the contrary, in CGM all the tubes in a panel have the same maximum wall temperature.

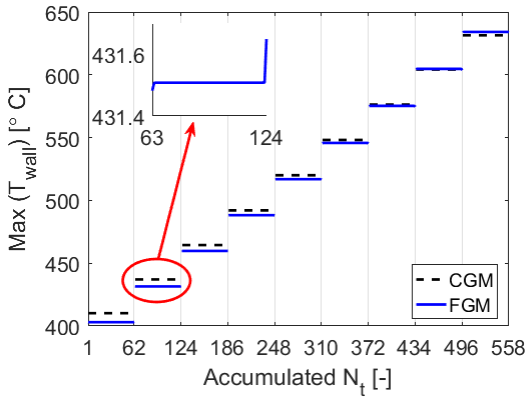

Figure 8 - Maximum wall temperature in each tube predicted by the CGM and the FGM for the case of a homogeneous incident flux of 0.3 MW/m².

The maximum tube wall temperature is one of the main limiting restrictions of the receivers, since it is responsible of the molten salt decomposition and the tube corrosion. For a given molten salt temperature at the outlet of the receiver, the homogeneous incident flux must be different in the CGM and the FGM if they have the same maximum tube wall temperature in the whole receiver. Figure 9.a depicts the maximum temperature of the tubes for a same maximum temperature in the whole receiver of 634.1 °C. This maximum temperature for the whole

receiver corresponds to the same incident solar flux as before for the FGM (0.3 MW/m^2) and to 0.317 MW/m^2 for the CGM. The new mass flow rate for CGM is 152.6 kg/s, which is still lower than the mass flow rate of the FGM (162.2 kg/s).

Although in the last panel of the receiver the tube wall temperature must be exactly the same, the differences between the CGM and the FGM temperatures in the first panels have increased with respect to the case of the same uniform heat flux. In the first panel the temperature gradient in the tube walls is the highest and hence in this panel the thermal stresses are another limiting parameter of the receivers. Figure 9.b shows the maximum thermal stresses in each tube of the receiver (Equation 13) calculated with the CGM and the FGM. As can be seen in the Figure, for these homogeneous solar flux distributions that lead to the same maximum wall temperature in the whole receiver (at panel 9), the CGM yields the highest thermal stresses in each of the tubes of the receiver.

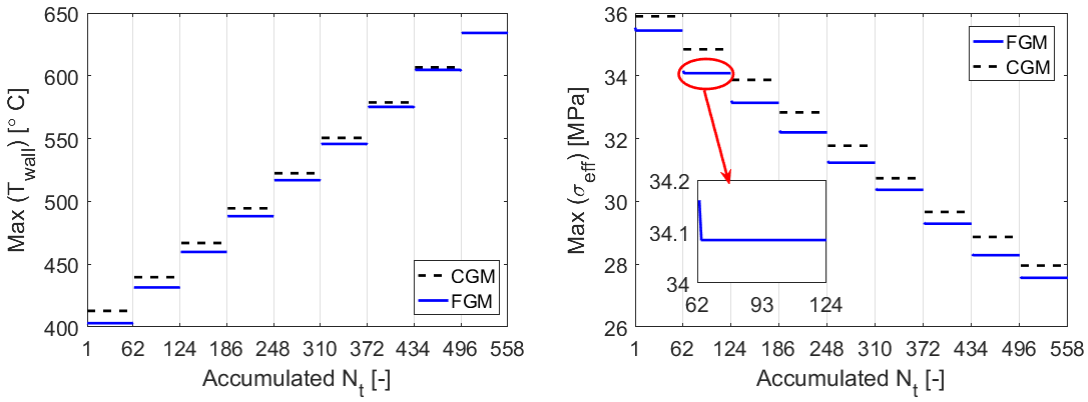

Figure 9 - (a) Maximum wall temperature in each tube and (b) Maximum thermal stress in each tube for the case of uniform incident fluxes (0.317 MW/m^2 in CGM and 0.3 MW/m^2 in FGM) set to obtain a maximum wall temperature in the whole receiver equal to 634.1 °C.

Finally, the difference between the mass flow rate and the heat in the CGM and the FGM in all the cases analysed implies that both models lead to unequal thermal efficiencies. In particular, under this unrealistic uniform flux distribution, the CGM and the FGM yield a receiver efficiency of 79.76% and 84.58%., respectively. This means that the CGM underestimates the thermal efficiency of the receiver by 4.8% with respect to the more precise FGM. Table 2 shows a summary of the data obtained during the receiver analysis with homogeneous incident solar flux distribution.

Table 2- Main results of the different cases analysed

	Model	q''_{field} [MW/m^2]	$\max(T_{wall})$ [°C]	$\dot{m}$ [kg/s]	$\max(\sigma_{eff})$ [MPa]	η_{rec} [%]
Same incident solar flux	CGM	0.3	631.4	143.6	34.02	75.06
	FGM	0.3	634.1	162.2	35.44	84.58
Same maximum wall temperature	CGM	0.317	634.1	152.6	35.90	79.76
	FGM	0.3	634.1	162.2	35.44	84.58

4.2. Model comparison for the case of a real aiming strategy

To perform a realistic receiver simulation, the influence of non-homogenous incident solar flux is studied in this section. The analysis is done on the Spring Equinox at solar noon, the typical design point of solar tower receivers. Here several aiming strategies are used to observe the differences between both models. The aiming strategies are characterized by an aiming factor, *k*, as explained in (Sánchez-González et al., 2018). The *k* factor is comprised between 3 and 0, with 3 being equivalents to an equatorial aiming strategy and 0 being equivalent to an aiming of all the heliostats to the upper and lower edges of the receiver. Low *k* factors reduce the solar peak flux, but increase the spillage losses and hence reduce the average incident solar flux and the optical efficiency of the solar field.

Figure 10 shows an example of the incident solar flux distribution on the receiver surface for *k*=2 using the CGM (left side) and the FGM (right side). Although the average flux distribution in each panel is set to be the same for the CGM and the FGM, the local distribution of the heat flux differs because the higher resolution of the FGM allows a heat flux variation from tube to tube of the same panel.

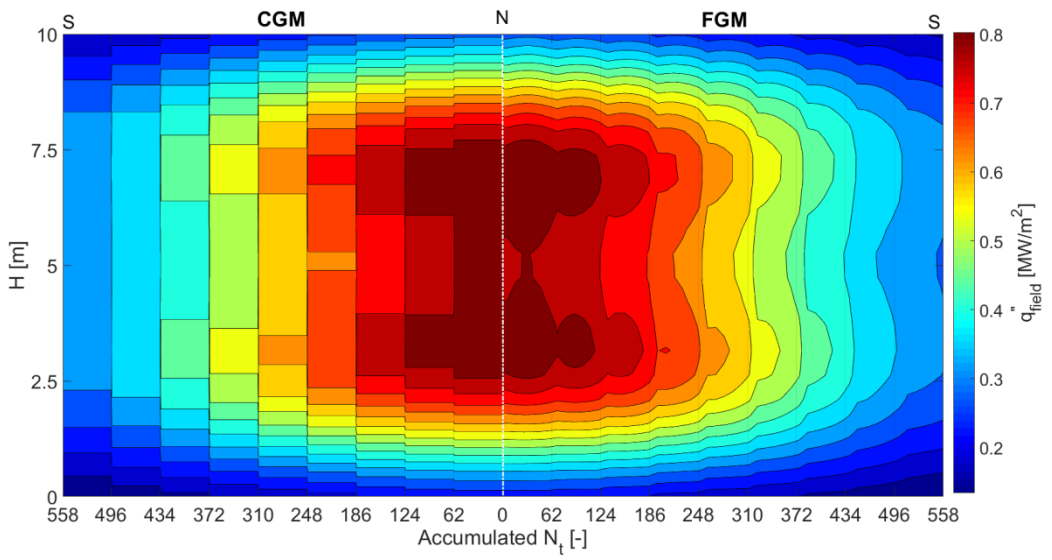

Figure 10- Incident solar flux distribution on the receiver surface for k=2 in the CGM (left side) and the FGM (right side).

For the incident solar flux distribution of Figure 10, Figure 11 depicts the frontal tube wall temperature distribution (θ=0°) obtained with the CGM (left side) and the FGM (right side). In Figure 11 it can be seen that the wall temperature is higher in the last panels (exit) than in the first panel (inlet) of the receiver. Therefore, the tube temperature is more affected by the molten salt temperature than by the distribution of incident heat flux. Besides, in the odd panels (up flow) the temperature is higher close to the top edge of the tubes and vice versa in the even panels (down flow). In the CGM there are no differences between tubes of the same panel. On the contrary, in the FGM the tubes at the beginning of one panel have higher temperature than the tubes at the end of that panel; this effect is due to the incident solar flux, which decreases from north to south. Between both models, noticeable differences can be found in the different panels, i.e. the peak temperature is 625.5 °C in the CGM and 634.6 °C in the FGM.

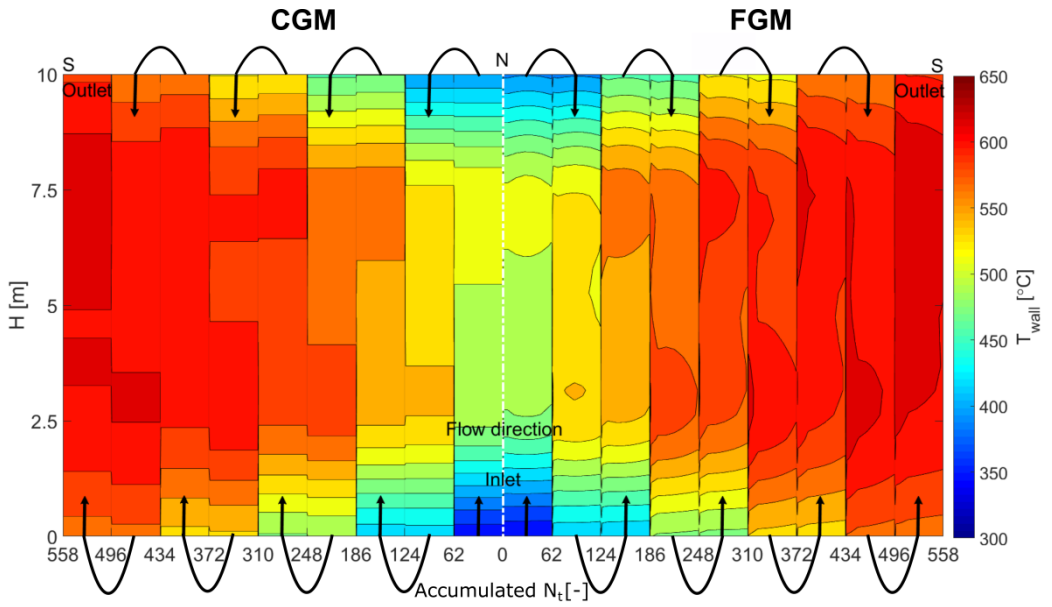

Figure 11- Tube wall temperature distribution in the frontal part of the tubes (θ=0°) for k=2 in the CGM (left side) and the FGM (right side). The arrows indicate the molten salt paths in the receiver.

Figure 12 shows the evolution of the different variables with the aiming factor: mass flow rate, maximum wall temperature, maximum thermal stress, receiver efficiency and combined field-receiver efficiency as a funtion of the aiming strategy employed, when the receiver operates between 290 °C and 565 °C. All the variables obtained with the FGM are higher than the ones obtained with the CGM. However, the evolution of the variables with the aiming factor is similar for both models. Exception of this is the receiver efficiency, which varies with *k* slightly more in the CGM than in the FGM. In general, the magnitudes of all the variables, excepting the temperature, increases with the aiming factor, but with different slope. The lowest maximum wall temperature in the whole receiver corresponds to *k*=1.5 instead of *k*=1. Although, the spillage losses are lower in *k*=1.5 than in *k*=1 (higher average heat flux), the flux distribution in *k*=1.5 is more homogeneous than in *k*=1, see (Rodríguez-Sánchez et al., 2018), and then the peak flux and then the maximum wall temperature in the whole receiver are lower. For the receiver analysed and a given aiming factor, the CGM underestimates the maximum wall temperature and the thermal stresses of the whole reciever around 10 °C and 3MPa, respectively. Besides, CGM underestimates the mass flow rate of molten salt and the combined field-receiver efficiency in 21.4 kg/s and 3.6%.

In the receiver operation, the critical parameter is not the aiming factor, but the maximum wall temperature in the shole receiver, which must be fixed to avoid damage in the receiver. The

difference between the CGM and the FGM variables will depend on the selected maximum wall temperature in the whole receiver.

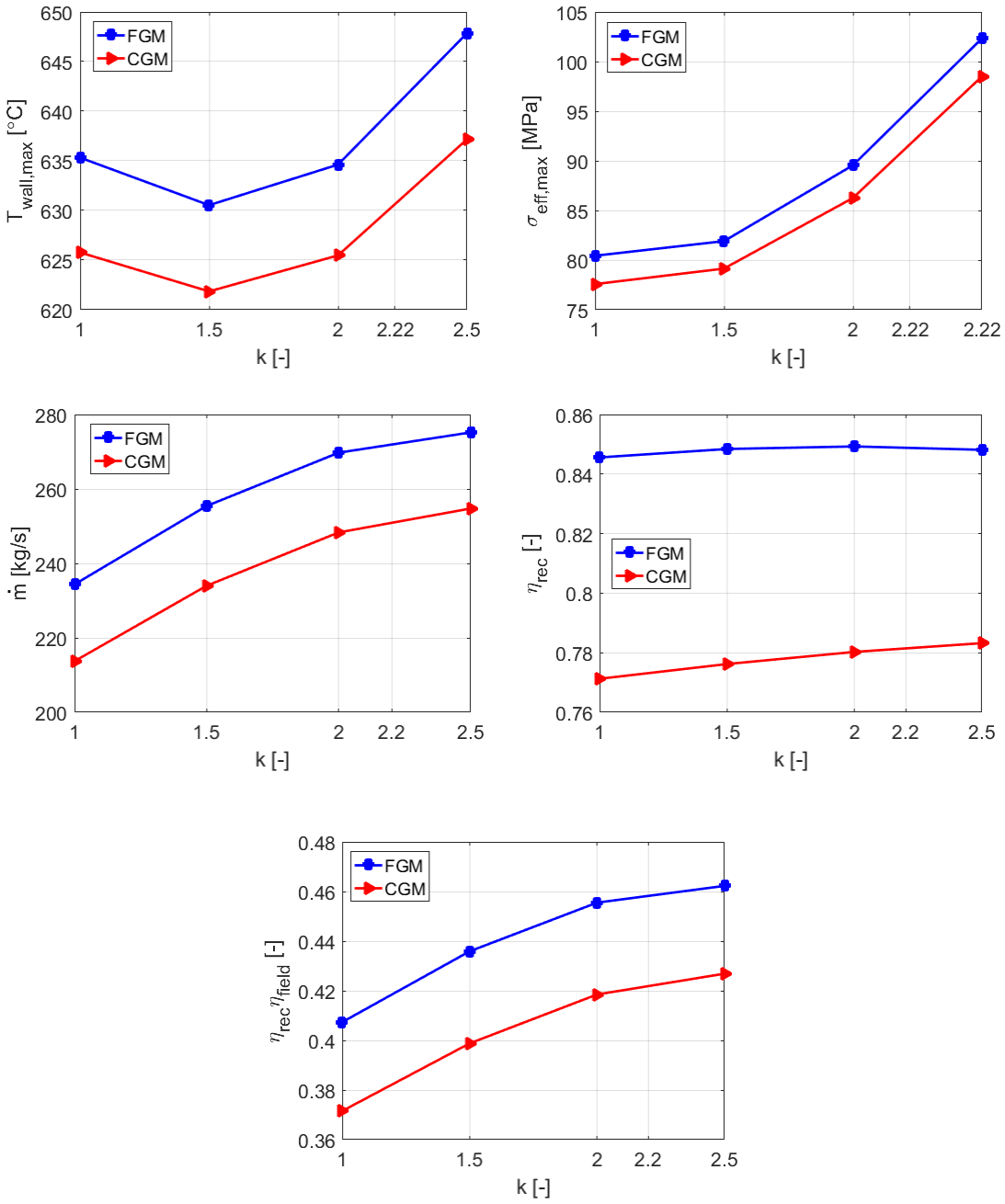

Figure 12 - Evolution of the maximum wall temperature, maximum thermal stresses, mass flow rate, receiver efficiency and combined field-receiver efficiency as a function of the aiming factor.

For the tube material analysed here, the maximum allowable wall temperature in the whole receiver is around 631 °C. This temperature corresponds to an aiming factor 1.5 in the FGM and 2.2 in the CGM. Therefore, the CGM is unable to predict with an acceptable accuracy the aiming factor that fulfills the limits of operation. Thus, if *k*=2.2 is used the corrosion and the stresses

can be fateful for the receiver according to the more precise result obtained with the FGM (640 °C and 95 MPa).

At 631 °C temperature (k=2.2), the CGM predicts a thermal efficiency of the receiver of 78.1%, which is 6.7% lower than the more refined perdiction of the FGM. However, the combined field-receiver efficiency according to the CGM is only 2% lower than the one determined with the FGM. Therefore, the innacuracy of the CGM, concerning the receiver efficiency calculation, is compensated by the variation of the solar field efficiency with the innacurate aiming factor.

In other words, when the maximum allowable tube wall temperature is modified, the prediction of the different variables by the models also varies. However, in all the cases the aiming factor selected in CGM modifies the solar field efficiency and this variation compensates the variation of the receiver efficiency. Therefore, although the individual efficiencies are not well calculated with CGM, the product of both efficiencies is only 2-2.5% different than the combined efficiency obtained with the FGM. Hence, the CGM can predict the annual power generation of a SPT with low grade of error. Note that the receiver and the field efficiencies are coupled because the maximum temperature increment of the salt and the tube wall temperature are kept constant in the operation of the receiver. Therefore, given an aiming strategy, there is only one possible receiver efficiency.

Computational time

The computational time to convergence of the CGM and the FGM for the receiver described above is 15 and 15000 s, respectively. This reference time was obtained using a standard PC equipped with an Intel quad-processor and 4GB of RAM. Thus, the computational time of the FGM is three orders of magnitude higher than that of the CGM. This increase of the computational time is higher than the increase in the number of tubes that have to be solved, from 18 in the CGM to 1116 in the FGM. Therefore, the increase of the computational time is also related with the interaction between panels.

5. Conclusions

This research shows that it is essential to ensure a sub-panel resolution of the incident solar flux on the receiver surface, in order to accurately model the thermo-mechanical behaviour of solar central receiver. To this aim, a new thermo-mechanical model to describe the behaviour of the solar external receiver has been developed, which is based in a fine grid resolution of the incident radiation. This new "*fine grid model"* (FGM) solves the circumferential variation of the heat absorbed by the tubes and their temperatures using a description of the incident radiation

given by cells of width equal to the tube pitch. In this way the FGM is able to obtain the temperature profiles and the thermal stresses in all the tubes of a given panel of the receiver.

The FGM has been compared with a lower resolution "*coarse grid model*" (CGM), whose incident radiation is described with cells of width equal to the panel width. The results indicate that the CGM is very useful in the design of SPTs, because it generates a first approximation of the yield production of the power plant with an error lower than 2.5% in a quick way. However, the CGM is not able to predict damage on the receiver associated to the thermo-mechanical behaviour of the receiver.

According to the cases analysed, the CGM produces an underestimation of the tube wall temperature and of the thermal stress. This leads to an overestimation of the solar flux distribution on the receiver that is required for a safety receiver operation.

Therefore, to assure the correct operation of the solar power plant we suggest to use a model with sub-panel resolution of the incident radiation like the FGM here proposed. The FGM calculates with more accuracy the tube wall temperature and the thermal stresses in all the tubes of the receiver for a given set of conditions. This is essential to avoid damage in the receiver. Besides, the FGM improves the estimation of the individual efficiencies of the solar field and the receiver, which is crucial to select the most adequate aiming strategy for each irradiation conditions.

Acknowledgements

This work has been supported by the Spanish government under the projects ENE2015-69486-R (MINECO/FEDER, UE) and by the fellowship "Ayuda a la investigación en energía y medio ambiente" of the Foundation Iberdrola España to study the stresses and deformations in external solar receivers.

References

American Society of Mechanical Engineers, 2011. ASME Boiler and Pressure Vessel Code, Section II - Materials. American Society of Mechanical Engineers, New York.

Behar, O., Khellaf, A., Mohammedi, K., 2013. A review of studies on central receiver solar thermal power plants. Renew. Sustain. Energy Rev. 23, 12–39. doi:10.1016/j.rser.2013.02.017

Faupel, J.H., Fisher, F.E., 1981. Synthesis of Stress Analysis and Materials Engineering, 2nd ed. Wiley, New York.

Garcia, P., Ferriere, A., Bezian, J.-J., 2008. Codes for solar flux calculation dedicated to central receiver system applications: A comparative review. Sol. Energy 82, 189–197. doi:10.1016/j.solener.2007.08.004

Gatewood, B.E., 1940. Thermal Stresses in Long Cylindrical Bodies. Philos. Mag. 282–301.

Gauché, P., Rudman, J., Mabaso, M., Landman, W.A., von Backström, T.W., Brent, A.C., 2017. System value and progress of CSP. Sol. Energy. doi:10.1016/j.solener.2017.03.072

Gnielinski, V., 2013. On heat transfer in tubes. Int. J. Heat Mass Transf. 63, 134–140. doi:10.1016/j.ijheatmasstransfer.2013.04.015

Hernández-Moro, J., Martínez-Duart, J.M., 2013. Analytical model for solar PV and CSP electricity costs: Present LCOE values and their future evolution. Renew. Sustain. Energy Rev. 20, 119–132. doi:10.1016/j.rser.2012.11.082

Li, L., Li, Y., Sun, J., 2017. Prospective fully-coupled multi-level analytical methodology for concentrated solar power plants: Applications. Appl. Therm. Eng. 118, 159–170. doi:10.1016/j.applthermaleng.2017.02.094

Lilliestam, J., Labordena, M., Patt, A., Pfenninger, S., 2017. Empirically observed learning rates for concentrating solar power and their responses to regime change. Nat. Energy 2, 17094. doi:10.1038/nenergy.2017.94

Marugán-Cruz, C., Flores, O., Santana, D., García-Villalba, M., 2016. Heat transfer and thermal stresses in a circular tube with a non-uniform heat flux. Int. J. Heat Mass Transf. 96, 256–266. doi:10.1016/j.ijheatmasstransfer.2016.01.035

Modest, F.M., 2003. Radiative Heat Transfer, in: Radiative Heat Transfer. Elsevier science, New York, San Francisco, London, pp. 162–197.

Nithyanandam, K., Pitchumani, R., 2016. Thermal and structural investigation of tubular supercritical carbon dioxide power tower receivers. Sol. Energy 135, 374–385. doi:10.1016/j.solener.2016.05.039

Rodríguez-Sánchez, M.R., Marugan-Cruz, C., Acosta-Iborra, A., Santana, D., 2014a. Comparison of simplified heat transfer models and CFD simulations for molten salt external receiver. Appl. Therm. Eng. 73, 991–1003. doi:10.1016/j.applthermaleng.2014.08.072

Rodríguez-Sánchez, M.R., Sánchez-González, A., Marugan-Cruz, C., Santana, D., 2015. Flow patterns of external solar receivers. Sol. Energy 122, 940–953. doi:10.1016/j.solener.2015.10.025

Rodríguez-Sánchez, M.R., Sánchez-González, A., Santana, D., 2018. Feasibility study of a new concept of solar external receiver: Variable velocity receiver. Appl. Therm. Eng. 128. doi:10.1016/j.applthermaleng.2017.08.173

Rodríguez-Sánchez, M.R., Soria-Verdugo, A., Almendros-Ibáñez, J.A., Acosta-Iborra, A., Santana, D., 2014b. Thermal design guidelines of solar power towers. Appl. Therm. Eng. 63, 428–438. doi:10.1016/j.applthermaleng.2013.11.014

Sánchez-González, A., Rodríguez-Sánchez, M.R., Santana, D., 2018. Aiming factor to flatten the flux distribution on cylindrical receivers. Submitt. Publ. to Energy.

Sánchez-González, A., Santana, D., 2015. Solar flux distribution on central receivers: a projection method from analytic function. Renew. Energy 74, 576–587.

Siebers, D.L., Kraabel, J.S., 1984. Estimating Convective Energy Losses From Solar Central Receivers. Sandia National Laboratories SAND84-8717, Livermore.

Yang, X., Yang, X., Ding, J., Shao, Y., Fan, H., 2012. Numerical simulation study on the heat transfer characteristics of the tube receiver of the solar thermal power tower. Appl. Energy 90, 142–147. doi:10.1016/j.apenergy.2011.07.006

Zavoico, A.B., 2001. Solar Power Tower: Design Basis Document. San Francisco, SAND2001-2100.